Structure and properties of equiatomic CoCrFeNiMn alloy fabricated by high-energy ball milling and spark plasma sintering

A.S. Rogachev [a, b, *], S.G. Vadchenko [a], N.A. Kochetov [a], S. Rouvimov [c], D.Yu Kovalev [a], A.S. Shchukin [a], D.O. Moskovskikh [b], A.A. Nepapushev [b], A.S. Mukasyan [c]

[a] *Mezhanov Institute of Structural Macrokinetics and Materials Science Russian Academy of Sciences, Chernogolovka, Russia*
[b] *National University of Science and Technology "MISIS", Moscow, Russia*
[c] *Department of Chemical and Biomolecular Engineering, University of Notre Dame, Notre Dame, USA*

ARTICLE INFO

ABSTRACT

High-entropy alloy CoCrFeNiMn was produced by short high energy ball milling (90 min) and spark plasma sintering (10 min at 1073 K). Co-existence of two fcc-phases with lattice parameters 0.360 nm and 0.356 nm was demonstrated via HRTEM, XRD and other methods. The matrix fcc-phase with larger parameter transforms into the more compact phase during annealing up to 1273 K. Similar transformation partially occurs after SPS. Some elements, mostly Cr and Mn, released from the matrix phase and formed precipitates. Up to three types of precipitates, with characteristic size from 10-30 nm to 200−300 nm, have been detected and studied. Electric and thermal properties of the material, measured at room and elevated temperature, shown that lattice thermal conductivity plays an important role, along with free electron thermal conductivity.

1. Introduction

Multicomponent composition CoCrFeMnNi, often referred to as "Cantor Alloy", was the first equiatomic material [1] that delineated the new concept of high-entropy alloys (HEA) [2−4]. This five-elements composition persists to be in the focus of research works during last 15 years and became, perhaps, the most thoroughly studied system among dozens of HEAs [5,6]. Special interest in CoCrFeNiMn − based materials is due to their outstanding combination of properties, such as exceptional damage tolerance and fracture resistance, especially at cryogenic temperatures [7,8]; high tensile strenght and ductility [9−12]; superplasticity [13]; high hardness and strength [11,14,15]. Basic sub-alloys of this quinary HEA system also possess attractive properties: a medium-entropy alloy CoCrNi has exceptional damage tolerance at cryogenic temperatures [16], and nanocrystalline CoCrFeNi alloy demonstrates exceptional resistance to grain growth [17].

Along the accepted classification the CoCrFeNiMn belongs to a family of 3d transition metal HEAs with composition CoCrFeNiX, where X = Al, Ti, Cu, V, or Mn [5,6,18−20]. This family is based on the face-centered cubic (fcc) solid solution CoCrFeNi, which was commonly considered to be a thermally stable single phase [21−25]. However, recently the CoCrFeNi phase was reported to be thermally metastable at 1023 K [26]. After extensive annealing (800 h), tiny precipitates (fringes), a few nanometers long and about 0.1−0.3 nm thick, were found in the HEA matrix. These fringes, detected by TEM analysis, have the same fcc crystal structure as the matrix, but with a slightly different lattice parameter: 0.355 nm for the fringe, 0.366 nm for matrix [26]. Existence of two fcc phases with a lattice constant difference of 0.0001 nm was also reported for the as-casted CoCrFeNi alloy [27]. The fringes were hypothetically attributed to, so-called, Guinier−Preston (GP) zones that precede phase decomposition and formation of stable precipitates in aging alloys, but the chemical composition of the fringes was not determined.

Addition of a fifth alloying element with larger atomic radius

* Corresponding author. Mezhanov Institute of Structural Macrokinetics and materials Science Russian Academy of Sciences, Chernogolovka, Russia.
E-mail addresses: rogachev@ism.ac.ru (A.S. Rogachev), vadchenko@ism.ac.ru (S.G. Vadchenko), kolyan_kochetov@mail.ru (N.A. Kochetov), Sergei.Rouvimov.1@nd.edu (S. Rouvimov), kovalev@ism.ac.ru (D.Yu Kovalev), shchukin@ism.ac.ru (A.S. Shchukin), mos@misis.ru (D.O. Moskovskikh), anepapushev@gmail.com (A.A. Nepapushev), amoukasi@nd.edu (A.S. Mukasyan).

greatly accelerates the decomposition process. For example, when Al is added, Cr-rich precipitates typically form [26]. Since the radius of an Mn atom (0.137 nm) is close to that for Al (0.143 nm) and notably larger than the radii of the other four elements (0.124–0.125 nm), we may expect similar behavior for the CoCr-FeNiMn alloy. For a long time, this HEA composition was considered to be thermally stable: for example, after annealing at 1273 K for 3 days this alloy, according to XRD and SEM data, remained as a single-phase material [28]. However, during the last few years, the stability of this phase was disputed in several works [29–32]. First, some Cr-rich precipitates were observed along grain boundaries in the arc melted HEA after tensile tests at 1073 K (strain rate $2.56 \cdot 10^{-6}$ s^{-1}) [29]. In addition, several new nano-scale phases were found after 5 min annealing at 723 K, of the originally single-phase HEA, obtained by arc melting, drop casting and severe plastic deformation. Specifically, a NiMn phase and a Cr-rich phases formed and their volume fractions increased with increasing annealing time. In addition, a third FeCo phase precipitated after 1 h of such heat treatment [30]. Two types of precipitates were observed after long-term (1000h) heat treatment of the alloy at 1073 K, without application of any load [31]. The first type was a Cr-rich fcc phase, with a lattice parameter 1.06 nm, which corresponds to a $M_{23}C_6$ phase and was explained as contamination of melting equipment and initial powders with carbon. The second precipitated phase contained even more Cr, along with Mn, Fe and Co. This phase was found to be tetragonal, with lattice parameters of a ≈ 0.88 nm and c ≈ 0.45 nm, which is consistent with the σ phase [31]. Annealing for 500 days at 773–1173 K revealed both stable and unstable behavior at certain conditions [32]. It was shown that the alloy was a single-phase solid solution after homogenization for 2 days at 1473 K and remained in this state after a subsequent anneal at 1173 K for 500 days. However, a Cr-rich σ phase formed at 973 K, whereas three different phases (L10-NiMn, B2-FeCo, and a Cr-rich bcc phase) precipitated at 773 K [32]. Despite significant differences in the results obtained, all these works led to conclusion that CoCrFeNiMn can no longer be considered to be a thermodynamically stable single phase [31]. Contradictory reports can be found concerning the influence of precipitates on mechanical properties. On the one hand, the formation of Mn- and Cr-enriched precipitates weakens the mechanical strength of the CoCrFeNiMn HEA at elevated temperatures [29]. On the other hand, it was shown that nanostructured multiphase microstructure, consisting of MnNi, Cr-rich, and Fe-Co phases embedded in the HEA matrix, causes the hardening effect [30]. The precipitation hardening and strengthening were also reported for the fcc-HEA CoCrFeNi matrix, due to the formation of a nanosized coherent reinforcing phase L1$_2$-Ni$_3$(Ti,Al) [33].

The most common method for fabrication of CoCrFeNiMn alloy is an arc melting approach [29,31,32,34], that is often combined with subsequent hot rolling [9], cold rolling [10,35] or high-pressure torsion [30] of the ingots. Annealing is usually applied to as-cast and deformed materials. Alternative methods are: induction melting, plasma spray and laser cladding [36,37], mechanical alloying in a high-energy ball mill (HEBM), as well as the recently developed method of mechanical alloying by means of high-pressure torsion of a five-element mixture of fine metal powders [11]. Comparison of the arc-melted as-casted HEA with those, obtained via HEBM and consolidated by spark plasma sintering (SPS), have shown that the as-cast alloy had a much coarser microstructure, while mechanical properties were comparable [14]. Thus, the combination of HEBM + SPS may become one of the most efficient methods for fabrication of bulk HEA materials. Since SPS involves heat treatment at elevated temperature, questions concerning possible decomposition of HEAs and nature of the formed precipitate phases are of great importance. Also, it is worth noting that the

structure and properties of the CoCrFeNiMn HEA have been mostly studied for samples produced by melting.

In our previous work, we reported that single-phase CoCrFe-NiMn with an fcc structure (according to XRD and SEM) can be produced during 90 min of HEBM and consolidated by SPS [38]. Here we report the results on the fine structure, local composition, and the properties of dense bulk material on the base of CoCrFe-NiMn HEA produced by combination of HEBM + SPS methods.

2. Materials and methods

Metal powders of Co (purity >99.35%, particles size, d < 71 μm), Cr (>98.5%, d < 125 μm), Fe (>97%, size range 1.5–3.5 μm), Ni (>99.5%, d~30 μm) and Mn (>99.7%, d < 400 μm) were mixed in a mortar, in equimolar ratio. Then the mixture (10 g) was placed in a steel jar of a water-cooling planetary ball mill AGO-2 (ISSC SB RAS, Russia) together with steel balls (200 g, diameter 9 mm). Mechanical alloying was performed in air atmosphere, at rotating rate of the mill 912 rpm (jar rotated at 2220 rpm) for 5–120 min. It was shown that the single-phase CoCrFeNiMn with fcc structure formed after 90 min, hence all further investigated samples were prepared using 90 min of HEBM. It is critical to note that the powders milled for 15 min or longer became pyrophoric, that is fresh as-milled powders could self-ignite after opening the jar. To avoid this, the powders were kept in a closed jar during 24 h for natural passivation. The obtained powders were consolidated by means of SPS, using a Labox 650 (SinterLand, Japan). The powder was placed in a graphite press-die, heated in vacuum (15–20 Pa) at a rate of 100 K/s up to 1073 K and sintered at this temperature for 10 min under uniaxial loading (50 MPa). Disc-shaped samples of 30 mm in diameter and 5–6 mm thick were cut and polished for further tests.

The X-ray diffraction analysis of powders and sintered materials was performed with a DRON-3M diffractometer (Russia). In addition to Cu-K$_\alpha$ radiation (wavelength λ = 0.15419 nm), for better resolution we also used Fe-K$_\alpha$ (λ = 0.19374 nm) and Cr-K$_\alpha$ (λ = 0.22910 nm) radiation. High-temperature XRD measurements were made in vacuum 10^{-3} Pa, within the temperature range 298–1273 K using an ARL'XTRA diffractometer with high-temperature accessory HTK2000 "Anton Paar" (Switzerland). A crystal lattice distortion was determined by means of PDWin 6.0 software that used the method of second moments; instrumental lines broadening was determined with an LaB$_6$ standard (SRM 660b). The SEM and EDS studies were made using a Zeiss Ultra Plus field-emission scanning electron microscope (Carl Zeiss, Germany), equipped with an energy dispersive spectrometer INCA Energy 350 XT (Oxford Instruments, UK). Thin samples for TEM and STEM were prepared by means of a focused ion beam equipped Nanolab 6000 Helios Dual SEM/FIB (FEI, USA). For high resolution TEM and STEM we used a TITAN 800-300 TEM (FEI, USA) and a Thermis Z TEM equipped with DCOR + probe aberration corrector, monochromator and Super-X EDS technology (Thermo Fisher Scientific, USA).

Electrical resistivity was measured by a 4-point method with 15 × 2.8 × 0.88 mm plates cut from the sintered samples; thermal conductivity − by the flash-method using NanoFlash Netzsch LFA 447 (Germany); specific heat capacity was evaluated using a differential scanning calorimeter Mettler Toledo DSC-3. The Young modulus was measured by an ultrasound method; and microhardness with a PMT3 tester (Russia) at loading 50 g. The bending strength was measured by 3-point method with Instron testing machine.

3. Results

The XRD patterns for the initial powder mixture, after 60 and 90 min of HEBM and of the sintered alloy are shown in Fig. 1. It can
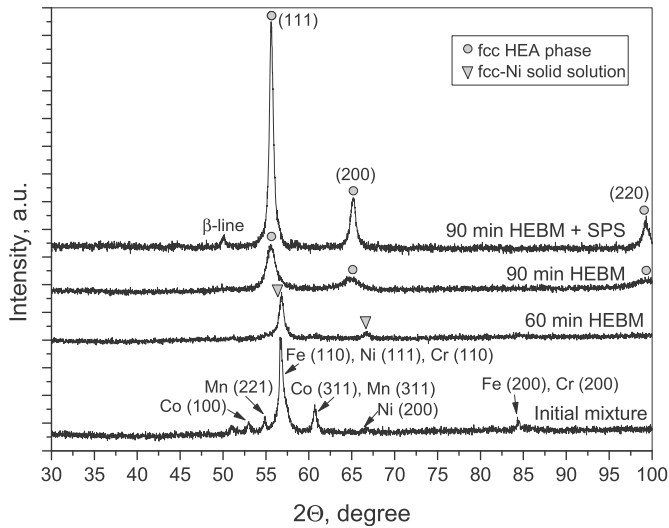
Fig. 1. Evolution of XRD patterns from initial mixture to consolidated material. Obtained with Fe-K$_\alpha$ radiation for better angle resolution.

be seen that the intensities of diffraction peaks of the initial metals gradually decreased with increasing duration of HEBM. After 60 min, the peaks of Co, Cr, Fe and Mn diminished to essentially background levels. The noticeable peaks belong to an fcc-phase with a lattice parameter $a = 0.3526$ nm, which is close to the lattice parameter of fcc-Ni (0.3524 nm, PDF card 000-04-0850). After 90 min of HEBM we observed sharp shifting of the XRD peaks toward smaller angles, manifesting formation of a phase with $a = 0.3604$ nm. After SPS, the fcc structure remained, diffraction peaks intensities increased, and the lattice parameter decreased to 0.3565 nm. Thus, we may conclude that after 60 min of HEBM the first fcc-phase forms as a solid solution of all metal components in the fcc-Ni, and after 90 min of mechanical treatment, this phase transforms into an HEA phase.

The mechanically alloyed powder was heated up to 1273 K with simultaneous XRD analysis, in order to study the thermal stability of the HEA phase. Evolution of XRD patterns, presented in Fig. 2,
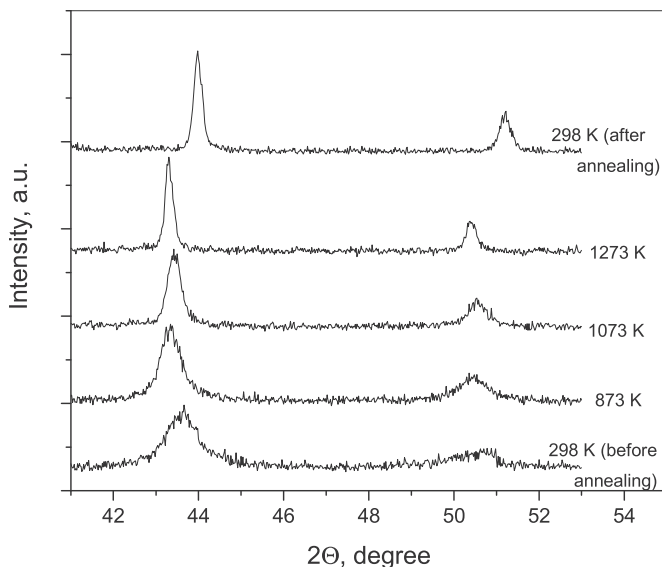
shows that the fcc structure remains during the heating up and cooling down. We did not observe any new phase or splitting of the diffraction peaks. However, the crystal lattice parameter changes during heat treatment (Fig. 3). Heating was carried out in a step-like manner with isothermal stages at 873, 1073, and 1273 K. Three sequential XRD patterns were acquired during each isothermal exposure and lattice parameters (a) and lattice distortion (δ) were determined from each pattern. It can be seen that the lattice parameter, a, increases with increasing temperature, but slightly decreases during isothermal stages. Increase of a occurs due to thermal expansion of the lattice, while its decrease may be explained by ordering and closer packing of atoms in crystal structure during annealing at constant temperature. The ordering effect is evident from the narrowing and growth of diffraction peaks (Fig. 2). Continuous decrease of lattice distortion may also be related to the relaxation of the crystal structure (Fig. 3). The structure shrinking effect diminished at 1273 K, hence we may assume that the lattice parameter reaches its equilibrium value at that temperature. The value of a before annealing was equal to 0.3595 nm, after annealing and cooling it decreased to 0.3565 nm. The thermal expansion coefficient was evaluated as $12 \cdot 10^{-6}$ 1/K in the beginning (heating from 298 to 873 K) and $15 \cdot 10^{-6}$ 1/K in the end of the experiment (cooling from 1273 to 298 K).

Morphology of the powder mixture undergoes significant changes in the process of HEBM (Fig. 4). Initial powders of very different sizes and shapes (Fig. 4,a) cold-welded into relatively large uniform particles with spongy surface after 60 min of treatment (Fig. 4,b). This powder, in turn, transformed into fragmented irregular particles after 90 min of HEBM (Fig. 4,c). TEM analysis of such particles, including the obtained electron diffraction patterns (EDP), shows that they primarily consist of nano-scale crystals of the fcc-phase with $a = 0.36$ nm (see Fig. 5,a and Table 1). Thorough analysis of HRTEM images reveals the existence of nano-crystallites with two slightly different d-spacings, 0.206 nm and 0.208 nm, as well some amorphous regions and distortions of the atomic planes (Fig. 6). In addition, some rounded precipitates, about 5–15 nm in diameter, were found with high resolution STEM (insert in Fig. 7,a). EDS analysis along the scan line is also presented in Fig. 7a. It can be seen that these precipitates are enriched with Cr (up to ~ 60 at.%) and depleted of all other components (below 10 at.%). Notable fluctuations of the EDS-determined local chemical composition can be observed in the matrix phase (Fig. 7a), i.e. the concentrations of
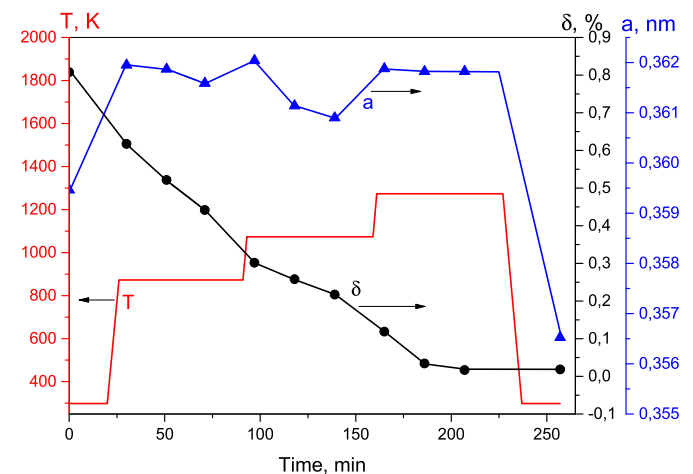

Fig. 2. High-temperature XRD patterns of the HEA powder (90 min HEBM; Cu-K$_\alpha$ radiation).

Fig. 3. (color online) Results of the high-temperature XRD experiments: temperature-time regime (T), crystal lattice distortion (δ, %) and lattice parameter (a, nm). (For interpretation of the references to color in this figure legend, the reader is referred to the Web version of this article.)
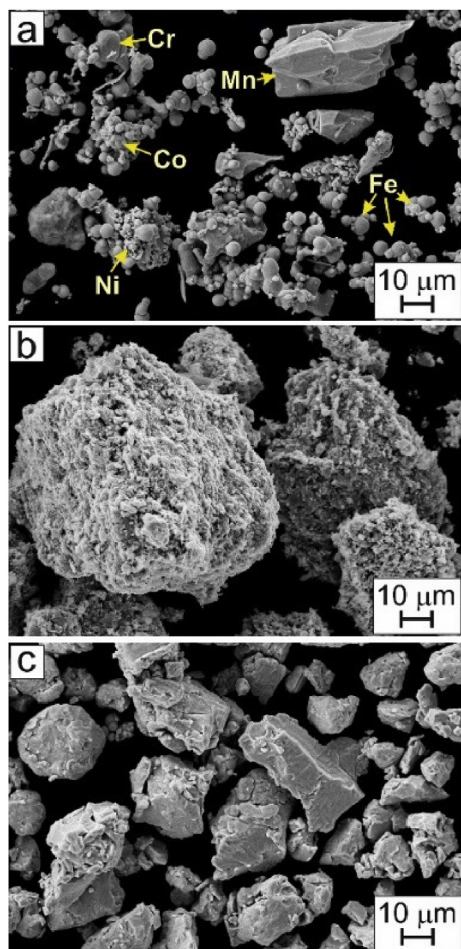
Fig. 4. SEM of the multicomponent powder blend: initial mixture of elemental powders (a); after 60 min of HEBM (b); after 90 min of HEBM (c).
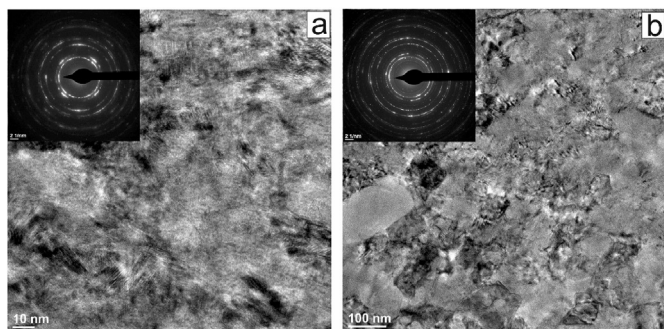

Fig. 5. TEM image and corresponding electron diffraction patterns: (a) - powder sample, after HEBM; (b) - compacted sample, after HEBM + SPS. Interpretation of the EDP is presented in Table 1.

Co and Cr vary within the range 17 ÷ 26 at.%, Fe within 18 ÷ 28 at.%, Ni 15 ÷ 21 at.%, and Mn 13 ÷ 25 at.%. Some part of these deviations may be related to the inaccuracy of the "standard-less" EDS analysis with extremely high space resolution; however, it is highly probable that nanometer-scale fluctuations of chemical composition occur in the HEA matrix.

Consolidation of the mechanically alloyed HEA powder was made by SPS at 1073 K for 10 min. The microstructure of the consolidated material looks completely uniform, without pores or composition deviations, in SEM (Fig. 8a). Etching of the polished cross-section in a mixture of strong acids (HCl + HNO₃, - so called "aqua-regia") developed boundaries between grains and some cavities that may be related to precipitates of a second phase (Fig. 8b). This microstructure shows that etching occurs mostly along grain boundaries, and size of the grains correlates with the size of powder particles after 90 min of HEBM (compare Figs. 4c and 8b). Results of EDS analysis presented in Table 2 (average of 9 measurements) show that the composition of the consolidated sample is close to equimolar, with some minor excess of Fe and lack of Ni and Mn.

According to TEM and EDP analysis of the consolidated materials, the size of microstructure elements increased after SPS, and additional electron diffraction lines appeared (Fig. 5b and Table 1). These additional lines can be roughly attributed to an fcc structure with $a = 1.05$ nm. Comparison of the Fig. 5a and 5,b shows, that after SPS some relatively large inclusions of up to 200−300 nm in size, that were not found in the powder particles after HEBM, forms in addition to previously existing small (~10 nm) precipitates. The existence of different types of precipitates in the consolidated material was confirmed by HAADF-STEM images in combination with X-ray mapping (Fig. 9) and high-resolution EDS scanning along the line (Fig. 7,b). Two types of inhomogeneities are prevalent. First, relatively large (up to 200 nm) Cr-rich inclusions that contain a few percent of Mn and practically zero Co, Fe, or Ni. Second, smaller (10−30 nm) rounded precipitates that contain all five elements. Line-scan EDS analysis shows that the precipitates contain slightly more Cr and Mn (25 ÷ 30 at.%) and less Fe, Ni and Co (13 ÷ 16 at.%). The matrix contains 16 ÷ 27 at.% of Fe and Ni, 11 ÷ 22 at.% Co, 10 ÷ 15 at.% Cr, and 15 ÷ 25 at.% Mn (approximate ranges). Therefore, we can conclude that after SPS the composition of small precipitates becomes more uniform with matrix phase, however, a small amount of large precipitates appear that contain a higher concentration of Cr. If the Cr-rich precipitates are undesirable phases, the content of this metal should be decreased, which may help to avoid precipitation. However, variation of the metal ratio requires additional research, in order to avoid altering composition of the matrix phase.

HRTEM study of the matrix phase confirms the co-existence of two fcc phases with close lattice parameters (Fig. 10). Perhaps, one of them pertains to the small precipitates, and another − to the matrix itself. Nano-twins were observed in the fcc phase with $a = 0.360$ nm (Fig. 10,b). Atomic packing inside the large precipitates does not conform to an fcc phase, as evident from Fig. 11 and Fig. 12. The crystal structure of this phase is a topic for further discussion.

Some experimentally measured properties of the consolidated material are presented in Fig. 13, as a function of temperature. As expected, thermal diffusivity and electrical conductivity are several times less than corresponding values for pure metals, while specific heat capacity is comparable with initial components. The material has an average density of 7.5 g/cm³, microhardness 4.03 ± 0.48 GPa and flexural (bending) strength 919 ± 20 MPa. The Young modulus and Poisson ratio (ultrasonic measurements) were found to be 184 GPa and 0.3, correspondingly.

4. Discussion

There are three main topics for discussion concerning bulk CoCrFeNiMn HEA: formation routes, stability, and properties. The combination of mechanical alloying and spark plasma synthesis is a relatively new approach for fabrication of HEAs, the casting-based methods are used much more often. Up to now, this approach has been demonstrated in a few works [14,38,39]. The results show the strong influence of the mechanical alloying regime on phase

Table 1
Interpretation of the Electron Diffraction Patterns presented in Fig. 5.

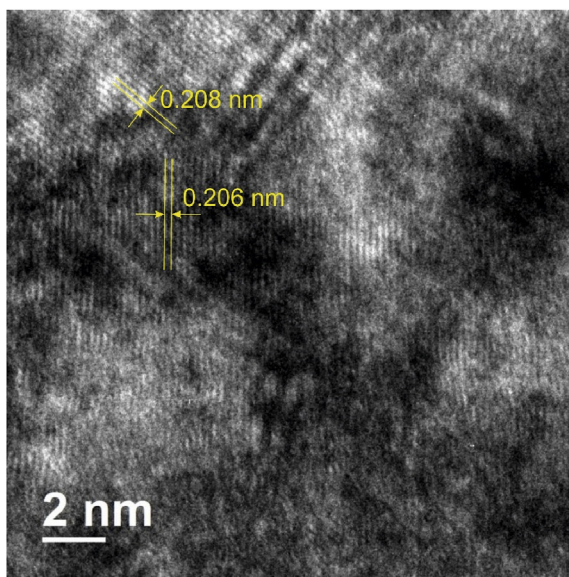| Experimental values				Possible interpretations		
After HEBM		After HEBM and SPS		Hypothetical structures: calculated d-spacings in nm, and (*hkl*)		
Ring diameter D, 1/nm	d-spacings nm	Ring diameter D, 1/nm	d-spacingsnm	fcc, $a = 0.36$ nm	fcc, $a = 1.05$ nm	bcc, $a = 0.73$ nm
		6.69	0.299	-	0.304 (222)	0.298 (211)
		7.88	0.254	-	0.258 (400)	0.258 (220)
9.62	0.208	9.62	0.208	0.208 (111)	-	0.211 (222)
11.04	0.181	11.27	0.177	0.180 (200)	-	0.182 (400)
		12.45	0.161	-	0.159 (622)	0.163 (420)
		13.28	0.151	-	0.152 (444)	0.156 (332)
						0.149 (422)
15.78	0.127	15.57	0.128	0.127 (220)	-	0.129 (440)
						0.125 (530), (433)
18.38	0.109	18.51	0.108	0.108 (311)	-	0.108 (631)

Fig. 6. HRTEM of the powder sample (after HEBM).

formation. Thus, 60 h required for obtaining mixture of fcc + bcc phases, when the rotating rate of planetary ball mill was 250 rpm [39]; the pure fcc phase was obtained after 8 h at 400 rpm [14]; while only 90 min was sufficient to obtain the same result at 912 rpm as shown in this work (see also [38]). In addition, we obtained an fcc-HEA powder without the addition of a process control agent (N-heptane) that was added to the mixture to avoid cold welding in the previous works [14,39]. The consolidation temperature used in the SPS method should be about $0.7 T_m$, where T_m is a melting temperature of the considered alloy. The experimentally measured melting temperature of the CoCrFeNiMn phase was reported as 1607 K [40,41], 1523 K [14], or 1543 K [42], while atomistic modelling predicted $T_m = 1679$ K [43]. Therefore, the temperature range 1070–1175 K may be considered to be an optimal for SPS (it can be noted that Mn lowers T_m of the 4-component basic alloy CoCrFeNi, which is 1717 K [41] or 1707 K [43]). A material with density of 7.5 g/cm^3 was obtained in the present work with SPS temperature 1073 K, which is slightly lower that the value 7.85 g/cm^3 achieved in the work [39] under similar conditions. The theoretical density for an equiatomic CoCrFeNiMn fcc-phase with lattice parameter 0.36 nm is equal to 8.03 g/cm^3. Therefore, if we presume that the consolidated materials are single-phase, they must have porosities of 2.24% for [39] and 6.6% in the
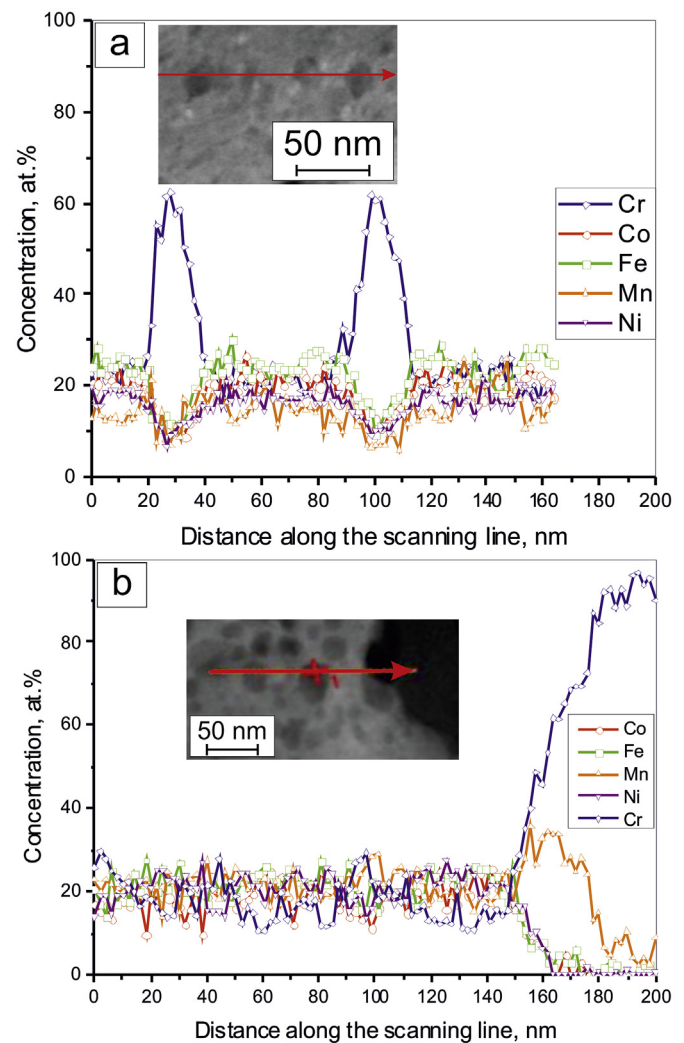

Fig. 7. EDS microanalysis along the scanning lines, that are shown by arrows on the inserted STEM pictures: (a) - powder sample, after HEBM; (b) - consolidated sample, after HEBM + SPS.

present work. These values are in a reasonable agreement with results from the work [14], where porosity was 7.61% after SPS at 1073 K and decreased to 0.12%, when SPS was carried out at 1273 K. However, our SEM study did not reveal residual porosity at polished
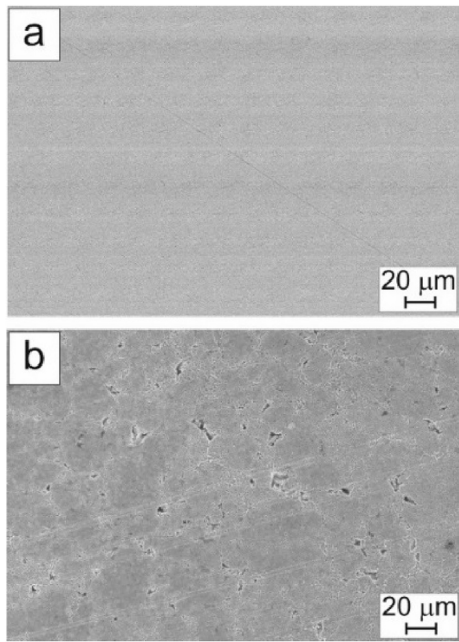
Fig. 8. SEM images of the consolidated sample (HEA + SPS): a - polished cross-section, Z-contrast (backscattered electrons, AsB detector); b — the same area after acid etching, image in secondary electrons. Results of EDS analysis are presented in Table 2.

Fig. 9. (color online) HAADF STEM microstructure image of the sample consolidated by SPS, with corresponding X-ray mappings. (For interpretation of the references to color in this figure legend, the reader is referred to the Web version of this article.)

cross-sections without etching (Fig. 8,a). Thus, we may conclude that the observed lower density occurs due to presence of different phases with lower theoretical densities.

Despite the intense research into the phase stability and possible phase transformations in the Co-Cr-Fe-Ni-Mn system, this issue is still far from being resolved (see also Introduction). For cast equiatomic alloys, the fcc-solid solution with lattice parameter (a) 0.359 nm is commonly accepted as the major or sole phase. This a value was first obtained for a major dendritic phase in the pioneering work [1] and confirmed in many other works; e.g., precise neutron diffraction study shown $a = 0.3597$ nm, with error less than 0.00001 nm [42]. Shrinking of crystal lattice from a = 0.3602 nm to a = 0.3595 nm was observed earlier for as-cast and annealed (1273 K for 24 h) samples, respectively [34]. Mechanical alloying produces fcc-phases with $a = 0.3536 \pm 0.02$ nm [39], and $0.3595 \div 0.3604$ nm (present work, XRD and SAED data, — Figs. 1, Fig. 3, Fig. 5,a, Table 1). HRTEM (Fig. 4) shows co-existence of two phases in neighboring crystallites, with close lattice parameters: d-spacing 0.208 nm corresponds to an fcc phase with $a = 0.360$ nm, and d-spacing 0.206 nm — to $a = 0.356$ nm. Since the corresponding X-ray diffraction peaks are broadened and blurred due to intense plastic deformation and lattice distortions occurred during HEBM, it is hard to distinguish these phases, so they look like one fcc phase in XRD patterns (Fig. 1). However, transformation of the fcc-phase with larger a into an fcc-phase with smaller a can be clearly observed during annealing of the HEBM treated powder (Fig. 3). This transformation is accompanied by lattice relaxation and precipitate formation. Both phases, with larger and smaller a,
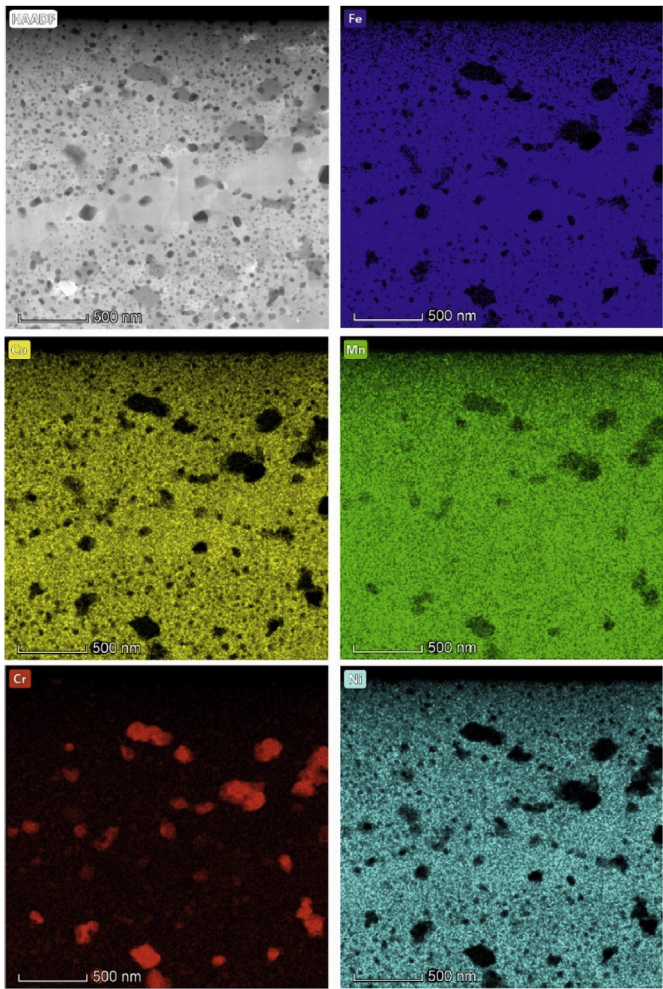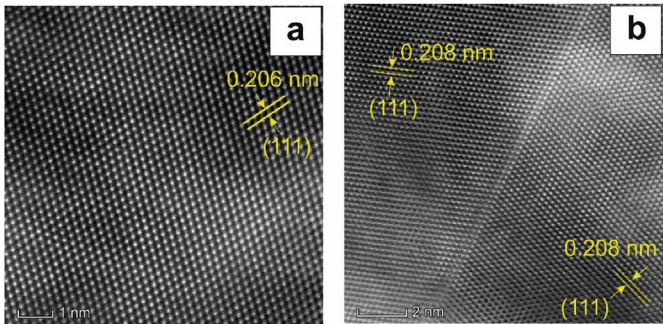

Fig. 10. HRTEM of the CoCrFeNiMn matrix phases: fcc phase with a = 0.356 nm (a) and fcc phase with a = 0.360 nm (b).

Table 2
EDS analysis of the compacted material (HEBM + SPS).

Polished cross section	Concentration, at. %				
	Co	Cr	Fe	Ni	Mn
Before etching	19.0 ± 0.8	21.4 ± 0.4	23.2 ± 1.2	18.6 ± 2.0	17.8 ± 1.7
After etching	18.8 ± 0.4	20.1 ± 1.0	22.8 ± 0.3	18.8 ± 0.4	19.1 ± 0.4
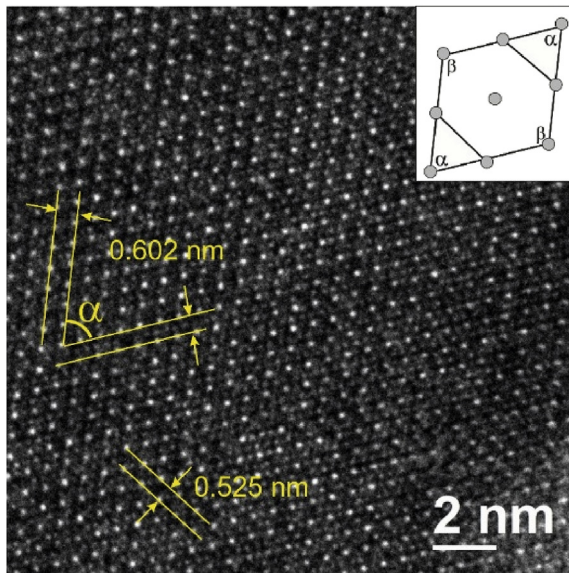
Fig. 11. HRTEM of the precipitated dispersed phase. Angles: $\alpha \approx 70°$, $\beta \approx 110°$.

Fig. 13. Temperature dependence of the specific electrical conductivity (σ), thermal diffusivity (χ) and specific heat capacity (c) of the consolidated (HEBM + SPS) HEA material.
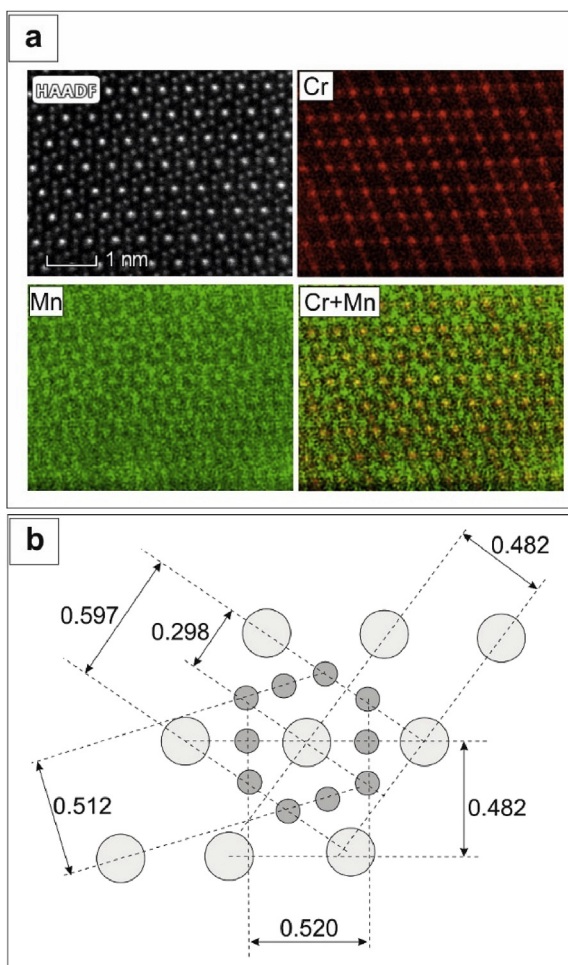

Fig. 12. (color online). Atomic structure of precipitate: HAADF STEM image with corresponding X-ray mappings (a), and principal lattice spacings (b). All dimensions are given in nanometers. (For interpretation of the references to color in this figure legend, the reader is referred to the Web version of this article.)
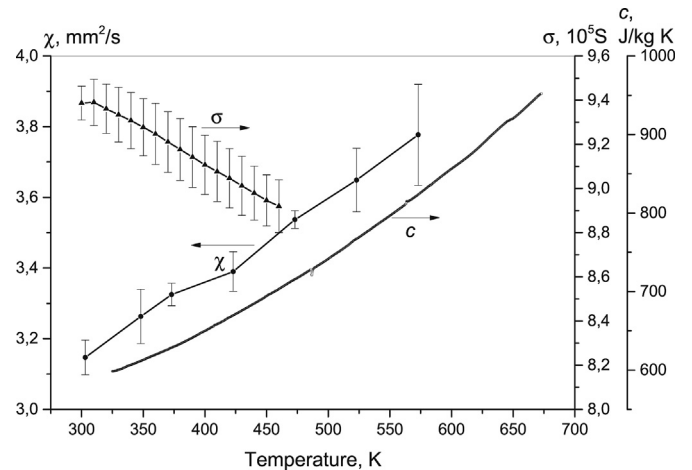
survive under the relatively soft annealing conditions (1073 K for 10 min) taking place during SPS, as shown in Fig. 10. On the other hand, two-phase (fcc + bcc) powder, obtained by HEBM, converted during SPS into a single fcc phase with $a = 0.3589-0.3590$ nm, as it was reported in the work [39]. From all these results, we can draw a conclusion, that two fcc phases with close lattice parameters co-exist in the HEA alloy after HEBM. The first of which has $a = 0.360 \pm 0.001$ nm, while for the second phase $a = 0.356 \pm 0.001$ nm. When annealing, the first phase tends to "unload" some elements, mostly Cr and Mn, which results in lattice relaxation and shrinking, and transformation into the second phase. The elements released from the first phase during this process form precipitates.

At least two types of precipitates were found in the material after SPS (Fig. 9). New diffraction lines appearing after SPS (Fig. 5,b and Table 1) can be interpreted as a fcc-phase with $a = 1.05$ nm, which is close to the structure of $Cr_{23}C_6$ ($a = 1.066$ nm). At the same time, the d-spacing and angles measured with HRTEM (Fig. 11) can be interpreted as a bcc structure with $a = 0.73$ nm. The electron diffraction lines calculated on the basis of this interpretation, exhibit reasonable agreement with experimental data (Table 1). Finally, a quite complicated structure was observed within the Cr-rich precipitates (Fig. 12). This structure possibly belongs to a binary $(Cr,Mn)C_x$-type carbide [44] or some not-recognized intermetallic phases in the Cr-Mn system. This question requires additional study.

The transport properties of the materials, presented in Fig. 13, show the significant role of lattice heat conductivity. It is known that for pure metals, when electric and heat conduction occur due to free electrons, the Wiedemann–Franz law describes the correlation between electrical and thermal conductivities:

$$\frac{\lambda}{\sigma} = LT, \tag{1}$$

where $L = 2.45 \cdot 10^{-8}$ W·Ohm/K^2 is the Lorenz number. Calculating thermal conductivity as $\lambda = c\rho\chi$ and substituting into eq. (1), we obtained $L \approx 4.5 \pm 0.2 \cdot 10^{-8}$ W·Ohm/K^2. Strictly speaking, within the temperature interval 350—573 K, the dependence of λ/σ on T can be described with the empirical equation $\lambda/\sigma = 12.68 - 0.0173T + 0.0000683T^2$ (W·Ohm/K). Such dependences lead us to conclude that transport of electric charges and heat occurs due to different carriers: electric current − by electrons, and

heat — by electrons plus phonons. Electrical resistivity of the material at room temperature is 106.5 μOhm·cm, which is about an order of magnitude larger than the resistivity of Co, Cr, Fe and Ni, but 2.6 times smaller than Mn. A coefficient of thermal expansion (CTE), $(34.2 \pm 0.2) \cdot 10^{-5}\,K^1$, is much less than for pure metals. These values are typical of multicomponent alloys and disordered solid solutions, because of intense electron scattering in its crystal lattice. Increase of electrical resistance and decrease of CTE were also reported for mechanically alloyed and SPS-consolidated Cu-Cr nanocomposites. In addition to the lattice disordering, this effect was also explained by the significant increase of specific surface of grain boundaries due to microstructure refinement [45]. Similar explanations can be suggested for the relatively low thermal conductivity (14–21 W/m·K at 350–573 K) and thermal diffusivity. The obtained values of electric and thermal conductivity are in a good agreement with data obtained earlier for the CoCrFeNi alloy: specific electric conductivity $(9.1–9.4) \cdot 10^5\,S$ for temperature range 300–400 K, and thermal conductivity 11–20.5 W/m·K for 298–573 K [46].

Mechanical properties of the materials exhibit less plasticity and more hardness than typical fcc-HEAs produced by crystallization of the melts, and comparable with ceramic-metal composites. Thus, the maximum flexural strength of TiB2-based cermet with HEA binder CoCrFeNiTiAl was 800 MPa, and Vickers hardness 23.56 GPa [47]. Possessing expectable lower hardness (microhardness 4 GPa, see Section 3), the HEA CoCrFeNiMn, studied in the current work, exceeds 900 MPa in flexural strength that is higher than the cermet material.

5. Conclusions

Due to great importance of HEAs for materials development [48], questions of their production routes, structures, stability, strengthening precipitates and properties, take on special significance.

High-entropy alloy CoCrFeNiMn was produced after 90 min of high energy ball milling and consolidated by spark plasma sintering at 1073 K for 10 min.

The as-milled alloy is composed of two fcc-phases with close lattice parameters, 0.360 nm and 0.356 nm. Both phases remain in the SPS-consolidated material, which was demonstrated via HRTEM and other methods.

The fcc-phase with the parameter 0.360 nm transforms into the more compact phase (0.356 nm) during annealing up to 1273 K. Similar transformation partially occurs after SPS. Some elements, mostly Cr and Mn, released from the matrix phase and formed precipitates.

Two or three types of precipitates, with characteristic size from 10 to 30 nm up to 200–300 nm, have been detected. Some of them have crystal structure close to $Cr_{23}C_6$, another possesses a complex crystal structure built of Cr and Mn atoms, that was not identified with any known intermetallic phase. Formation of a carbide phase may be possible because of SPS in a graphite die; thus, use carbon-free dies could be a way to avoid carbide precipitates. Further structural research is needed to decode structures of all precipitates.

Electric and thermal properties of the material are measured at room and elevated temperature. It is shown that lattice thermal conductivity plays an important role, along with free electron thermal conductivity.

Thus, the results obtained allow us to suppose that the recently formulated contradiction concerning stability of the CoCrFeNiMn high-entropy phase can be resolved, by accepting the existence of two fcc phases: metastable $(a = 0.360\,nm)$ and more stable $(a = 0.356\,nm)$.

References

[1] B. Cantor, I.T.H. Chang, P. Knight, A.J.B. Vincent, Microstructural development in equiatomic multicomponent alloys, Mater. Sci. Eng. A 375−377 (2004) 213−218.
[2] J.-W. Yeh, S.-K. Chen, S.J. Lin, J.-Y. Gan, T.-S. Chin, T.-T. Shun, C.-H. Tsau, S.-Y. Chang, Nanostructured high-entropy alloys with multiple principal elements: novel design concepts and outcomes, Adv. Eng. Mater. 6 (2004) 299−303.
[3] B. Cantor, Multicomponent and high entropy alloys, Entropy 16 (2014) 4749−4768.
[4] J.-W. Yeh, Physical metallurgy of high-entropy alloys, JOM 67 (10) (2015) 2254−2261.
[5] Y. Zhang, T.T. Zuo, Z. Tang, M.C. Gao, K.A. Dahmen, P.K. Liaw, Z.P. Lu, Microstructures and properties of high-entropy alloys, Prog. Mater. Sci. 61 (2014) 1−93.
[6] D.B. Miracle, O.N. Senkov, A critical review of high entropy alloys and related concepts, Acta Mater. 122 (2017) 448−511.
[7] B. Gludovatz, A. Honenwarter, D. Catoor, E.H. Chang, E.P. George, R.O. Ritchie, A fracture-resistant high-entropy alloy for cryogenic applications, Science 345 (2014) 1153−1158.
[8] Z.J. Zhang, M.M. Mao, J. Wang, B. Gludovatz, Z. Zhang, S.X. Mao, E.P. George, Q. Yu, R.O. Ritchie, Nanoscale origins of the damage tolerance of the high-entropy alloy CrMnFeCoNi, Nat. Commun. 6 (1−6) (2015) 10143.
[9] A. Gali, E.P. George, Tensile properties of high- and medium-entropy alloys, Intermetallics 39 (2013) 74−78.
[10] F. Otto, A. Dlouhy, Ch Somsen, H. Bei, G. Eggeler, E.P. George, The influence of temperature and microstructure on tensile properties of a CoCrFeMnNi high-entropy alloy, Acta Mater. 61 (2013) 5743−5755.
[11] A. Kilmametov, R. Kulagin, A. Mazilkin, S. Seils, T. Boll, M. Heilmaier, H. Hahn, High-pressure torsion driven mechanical alloying of CoCrFeMnNi high entropy alloy, Scr. Mater. 158 (2019) 29−33.
[12] C. Zhu, Z.P. Lu, T.G. Nieh, Incipient plasticity and dislocation nucleation of FeCoCrNiMn high-entropy alloy, Acta Mater. 61 (2013) 2993−3001.
[13] H. Shahmir, J. He, Z. Lu, M. Kawasaki, T.G. Langdona, Evidence for superplasticity in a CoCrFeNiMn high-entropy alloy processed by high-pressure torsion, Mater. Sci. Eng. 685 (2017) 342−348.
[14] F. Prusa, A. Senkova, V. Kucera, J. Capek, D. Vojtech, Properties of high-strength ultrafine-grained CoCrFeNiMn high-entropy alloy prepared by short-term mechanical alloying and spark plasma sintering, Mater. Sci. Eng. A 734 (2018) 341−352.
[15] S.J. Sun, Y.Z. Tian, H.R. Lin, X.G. Dong, Y.H. Wang, Z.J. Zhang, Z.F. Zhang, Enhanced strength and ductility of bulk CoCrFeMnNi high entropy alloy having fully recrystallized ultrafine-grained structure, Mater. Des. 133 (2017) 122−127.
[16] B. Gludovatz, A. Honenwarter, K.V.S. Thurston, H. Bei, Z. Wu, E.P. George, R.O. Ritchie, Exceptional damage-tolerance of a medium-entropy alloy CrCoNi at cryogenic temperatures, Nat. Commun. 7 (1−8) (2016) 10602.
[17] S. Praveen, J. Basu, S. Kashyap, R.S. Kottada, Exceptional resistance to grain growth in nanocrystalline CoCrFeNi high entropy alloy at high homologous temperatures, J. Alloy. Comp. 662 (2016) 361−367.
[18] W. Ji, Z. Fu, W. Wang, H. Wang, J. Zhang, Y. Wang, F. Zhang, Mechanical alloying synthesis and spark plasma sintering consolidation of CoCrFeNiAl high-entropy alloy, J. Alloy. Comp. 589 (2014) 61−66.
[19] D.Y. Li, Y. Zhang, The ultrahigh charpy impact toughness of forged Al$_x$CoCrFeNi high entropy alloys at room and cryogenic temperatures, Intermetallics 70 (2016) 24−28.
[20] S. Mohanty, T.N. Maity, S. Mukhopadhyay, S. Sarkar, N.P. Gurao, S. Bhowmick, Powder metallurgical processing of equiatomic AlCoCrFeNi high entropy alloy: microstructure and mechanical properties, Mater. Sci. Eng. A 679 (2017) 299−313.
[21] Y.-F. Kao, T.-J. Chen, S.-K. Chen, J.-W. Yeh, Microstructure and mechanical property of as-cast, -homogenized, and -deformed AlxCoCrFeNi (0<x<2) high-entropy alloys, J. Alloy. Comp. 488 (2009) 57−64.
[22] S. Guo, C. Ng, J. Lu, C.T. Liu, Effect of valence electron concentration on stability of fcc or bcc phase in high entropy alloys, J. Appl. Phys. 109 (2011) 103505.
[23] S. Guo, C.T. Liu, Phase stability in high entropy alloys: formation of solid solution phase or amorphous phase, Prog. Nat. Sci. 21 (2011) 433−446.

[24] M.S. Lucas, G.B. Wilks, L. Mauger, J.A. Munoz, O.N. Senkov, E. Michel, J. Horwath, S.L. Semiatin, M.B. Stone, D.L. Abernathy, E. Karapetrova, Absence of long-range chemical ordering in equimolar FeCoCrNi, Appl. Phys. Lett. 100 (2012) 257907.

[25] A.K. Singh, A. Subramanian, On the formation of disordered solid solutions in multicomponent alloys, J. Alloy. Comp. 587 (2014) 113–119.

[26] F. He, Z. Wang, Q. Wu, J. Li, J. Wang, C.T. Liu, Phase separation of metastable CoCrFeNi high entropy alloy at intermediate temperatures, Scr. Mater. 126 (2017) 15–19.

[27] U. Dahlborg, J. Cornide, M. Calvo-Dahlborg, T.C. Hansen, A. Fitch, Z. Leong, S. Chambreland, R.R. Goodall, Structure of some CoCrFeNi and CoCrFeNiPd multicomponent HEA alloys by diffraction techniques, J. Alloy. Comp. 681 (2016) 330–341.

[28] F. Otto, Y. Yang, H. Bei, E.P. George, Relative effects of enthalpy and entropy on the phase stability of equiatomic high-entropy alloys, Acta Mater. 61 (2013) 2628–2638.

[29] J.Y. He, C. Zhu, D.Q. Zhou, W.H. Liu, T.G. Nieh, Z.P. Lu, Steady state flow of the FeCoNiCrMn high entropy alloy at elevated temperatures, Intermetallics 55 (2014) 9–14.

[30] B. Schuh, F. Mendez-Martin, B. Volker, E.P. George, H. Clemens, R. Pippan, A. Hohenwarter, Mechanical properties, microstructure and thermal stability of nanocrystalline CoCrFeMnNi high-entropy alloy after severe plastic deformation, Acta Mater. 96 (2015) 258–268.

[31] E.J. Pickering, R. Minoz-Moreno, H.J. Stone, N.G. Jones, Precipitation in the equiatomic high-entropy alloy CrMnFeCoNi, Scr. Mater. 113 (2016) 106–109.

[32] F. Otto, A. Dlouhý, K.G. Pradeep, M. Kubĕnová, D. Raabec, G. Eggeler, E.P. Georgea, Decomposition of the single-phase high-entropy alloy CrMnFeCoNi after prolonged anneals at intermediate temperatures, Acta Mater. 112 (2016) 40–52.

[33] J.Y. He, H. Wang, H.L. Huang, X.D. Xu, M.W. Chen, Y. Wu, X.J. Liu, T.G. Nieh, K. An, Z.P. Lu, A precipitation-hardened high-entropy alloy with outstanding tensile properties, Acta Mater. 102 (2016) 187–196.

[34] G.A. Salishchev, M.A. Tikhonovsky, D.G. Shaysultanov, N.D. Stepanov, A.V. Kuznetsov, I.V. Kolodiy, A.S. Tortika, O.N. Senkov, Effect of Mn and V on structure and mechanical properties of high-entropy alloys based on CoCrFeNi system, J. Alloy. Comp. 591 (2014) 11–21.

[35] P.P. Bhattacharjee, G.D. Sathiaraj, M. Zaid, J.R. Gatti, C. Lee, C.-W. Tsai, J.-W. Yeh, Microstructure and texture evolution during annealing of equiatomic CoCrFeMnNi high-entropy alloy, J. Alloy. Comp. 587 (2014) 544–552.

[36] B. Gludovatz, E.P. George, R.O. Ritchie, Processing, microstructure and mechanical properties of the CrMnFeCoNi high-entropy alloy, J. Met. 67 (2015) 2262–2270.

[37] K.K. Alaneme, M.O. Bodunrin, S.R. Oke, Processing, alloy composition and phase transition effect on the mechanical and corrosion properties of high-entropy alloys: a review, J. Mater. Res. Technol. 4 (2016) 384–393.

[38] N.A. Kochetov, A.S. Rogachev, A.S. Shchukin, S.G. Vadchenko, I.D. Kovalev, Mechanical alloying with partial amorphization of Fe–Cr–Co–Ni–Mn multicomponent powder mixture and its spark plasma sintering for compact high-entropy material production, in: Izvestiya Vuzov. Poroshkovaya Metallurgiya I Funktsional'nye Pokrytiya (Universities' Proceedings. Powder Metallurgy and Functional Coatings), vol. 2, 2018, pp. 35–42 (in Russ.), https://doi.org/10.17073/1997-308X-2018-2-35-42.

[39] W. Ji, W. Wang, H. Wang, J. Zhang, Y. Wang, F. Zhang, Z. Fu, Alloying behavior and novel properties of CoCrFeNiMn high-entropy alloy fabricated by mechanical alloying and spark plasma sintering, Intermetallics 56 (2015) 24–27.

[40] K.-Y. Tsai, M.-H. Tsai, J.-W. Yeh, Sluggish siffusion in Co-Cr-Fe-Mn-Ni high-entropy alloys, Acta Mater. 61 (2013) 4887–4897.

[41] M. Vaidya, S. Trubel, B.S. Murty, G. Wilde, S.V. Divinski, Ni tracer diffusion in CoCrFeNi and CoCrFeMnNi high entropy alloys, J. Alloy. Comp. 688B (2016) 994–1001.

[42] L.R. Owen, E.J. Pickering, H.Y. Playford, H.J. Stone, M.G. Tucker, N.G. Jones, An assessment of the lattice strain in the CrMnFeCoNi high-entropy alloy, Acta Mater. 122 (2017) 11–18.

[43] M.A. Gutierrez, G.D. Rodriguez, G. Bozzolo, H.O. Mosca, Melting temperature of CoCrFeNiMn high-entropy alloys, Comput. Mater. Sci. 148 (2018) 69–75.

[44] G.K. Tirumalasetty, C.M. Fang, J. Jansen, T. Yokosawa, M.F.J. Boeije, J. Sietsma, M.A. van Huis, H.W. Zandbergen, Structural tale of two novel (Cr,Mn)C carbides in steel, Acta Mater. 78 (2014) 161–172.

[45] A.S. Rogachev, K.V. Kuskov, N.F. Shkodich, D.O. Moskovskikh, A.O. Orlov, A.A. Usenko, A.V. Karpov, I.D. Kovalev, A.S. Mukasyan, Influence of high-energy ball milling on electrical resistance of Cu and Cu/Cr nanocomposite materials produced by Spark Plasma Sintering, J. Alloy. Comp. 688A (2016) 468–474.

[46] H.P. Chou, Y.S. Chang, S.K. Shen, J.W. Yeh, Microstructure, thermophysical and electrical properties in Al$_x$CoCrFeNi ($0 \leq x \leq 2$) high-entropy alloys, Mater. Sci. Eng. B 163 (3) (2009) 184–189.

[47] W. Ji, J. Zhang, W. Wang, H. Wang, F. Zhang, Y. Wang, Z. Fu, Fabrication and properties of TiB2-based cermets by spark plasma sintering with CoCrFeNiTiAl high-entropy alloy as sintering aid, J. Eur. Ceram. Soc. 35 (2015) 879–886.

[48] D.B. Miracle, High entropy alloys as a bold step forward in alloy development, Nat. Commun. 10 (2019) 1805. https://doi.org/10.1038/s41467-019-09700-1.